NANO · MICRO small
www.small-journal.com

High-Yield Electrochemical Production of Large-Sized and Thinly Layered $NiPS_3$ Flakes for Overall Water Splitting

Xinzhe Li, Yiyun Fang, Jun Wang, Bin Wei, Kun Qi, Hui Ying Hoh, Qiaoyan Hao, Tao Sun, Zhongchang Wang, Zongyou Yin, Yupeng Zhang, Jiong Lu, Qiaoliang Bao, and Chenliang Su**

Achieving large-sized and thinly layered 2D metal phosphorus trichalcogenides with high quality and yield has been an urgent quest due to extraordinary physical/chemical characteristics for multiple applications. Nevertheless, current preparation methodologies suffer from uncontrolled thicknesses, uneven morphologies and area distributions, long processing times, and inferior quality. Here, a sonication-free and fast (in minutes) electrochemical cathodic exfoliation approach is reported that can prepare large-sized (typically ≈150 μm^2) and thinly layered (≈70% monolayer) $NiPS_3$ flakes with high crystallinity and pure phase structure with a yield ≈80%. During the electrochemical exfoliation process, the tetra-*n*-butylammonium salt with a large ionic diameter is decomposed into gaseous species after the intercalation and efficiently expands the tightly stratified bulk $NiPS_3$ crystals, as revealed by in situ and ex situ characterizations. Atomically thin $NiPS_3$ flakes can be obtained by slight manual shaking rather than sonication, which largely preserves in-plane structural integrity with large size and minimum damage. The obtained high quality $NiPS_3$ offers a new and ideal model for overall water splitting due to its inherent fully exposed S and P atoms that are often the active sites for hydrogen evolution reaction (HER) and oxygen evolution reaction (OER). Consequently, the bifunctional $NiPS_3$ exhibits outstanding performance for overall water splitting.

2D ternary metal phosphorus trichalcogenide (MPT) materials have received tremendous attention in recent years because of their distinctive structures and novel physical/chemical characteristics.[1] Among the MPTs, large-sized and thinly layered (LSTL) $NiPS_3$ flakes with high quality, which have distinctive properties due to an atomically thin structure, are the most sought-after materials in the scientific community. The remarkable charge–discharge performance, magnetic ordering property, intermediate range of bandgaps (≈1.6 eV), and preeminent electrochemical activity of this material, facilitate a wide range of applications in batteries,[2] electronics,[3] optoelectronics,[4] and catalysis.[5] However, despite tremendous effort, the production of LSTL $NiPS_3$ with high quality remains a formidable challenge because of production difficulties, i.e., the inability to produce on a large scale, at an acceptable expenditure and in a reproducible manner.

The chemical vapor deposition method reported by He and coworkers is the predominant approach for directly preparing LSTL $NiPS_3$ on a laboratory-scale.[4,5f] Unfortunately, the scope of this technique is limited because of the lack of large-scale fabrication and layer-controlled growth, and large number of defects (up to 7.6% S vacancies).[5f] Mechanical exfoliation using Scotch tape can produce $NiPS_3$ flakes with high quality and crystallinity; these

Dr. X. Li, Dr. Y. Fang, Dr. K. Qi, Dr. H. Y. Hoh, Dr. Q. Hao, Dr. Y. Zhang, Prof. C. Su
SZU-NUS Collaborative Center and International Collaborative Laboratory of 2D Materials for Optoelectronic Science & Technology of Ministry of Education
Engineering Technology Research Center for 2D Materials Information Functional Devices and Systems of Guangdong Province
Institute of Microscale Optoeletronics
Shenzhen University
Shen Zhen 518060, China
E-mail: chmsuc@szu.edu.cn

Dr. X. Li, Dr. Y. Fang, Dr. T. Sun, Prof. J. Lu
Department of Chemistry
National University of Singapore
3 Science Drive 3, Singapore 117543, Singapore

Dr. J. Wang, Dr. B. Wei, Prof. Z. Wang
Department of Quantum and Energy Materials
International Iberian Nanotechnology Laboratory (INL)
Avenida Mestre José Veiga s/n, Braga 4715-330, Portugal

Dr. K Qi, Dr. H. Y. Hoh, Dr. Y. Zhang, Prof. Q. Bao
Department of Materials Science and Engineering
ARC Centre of Excellence in Future Low-Energy Electronics Technologies (FLEET)
Monash University
Clayton, Victoria 3800, Australia
E-mail: qiaoliang.bao@monash.edu

Prof. Z. Yin
Research School of Chemistry
The Australian National University Canberra
Australian Capital Territory 2601, Australia

The ORCID identification number(s) for the author(s) of this article can be found under https://doi.org/10.1002/smll.201902427.

DOI: 10.1002/smll.201902427

flakes are mainly used for fundamental studies.[6] Nevertheless, practical applications of this method are greatly restricted because of the lack of scalability and random thickness and size of the obtained $NiPS_3$ flakes. Liquid-phase exfoliated bulk 2D crystals has recently emerged as an effective measure for preparing high-quality and atomically thin 2D flakes, such as Li intercalation,[1a,7] and ultrasonic methods.[8] The approach of Li intercalation requires large amount of time, and the process is extremely sensitive to ambient conditions. In addition, this approach may induce a phase transition, and the residual Li can promote a doping effect in the products. To date, the ultrasonic method is the unparalleled approach to harvest monolayer $NiPS_3$ flakes.[2,5a,b,d,e,9] Unfortunately, this method generally involves prolonged interaction of forces at all directions, ineluctably disintegrating the bulk crystals into an undersized area distribution (commonly <0.06 μm^2) with extensive defects, uneven morphology and inferior quality. Hence, the design and development of a feasible and scalable technique to produce large quantities of high-quality and solution-processable LSTL $NiPS_3$ is highly desired.

Herein, for the first time, we report the massive production of large-sized and monolayered $NiPS_3$ flakes with high quality by electrochemical cathodic exfoliation of bulk $NiPS_3$ crystals. The exfoliated $NiPS_3$ flakes have unprecedented sizes (area ≈ 150 μm^2) with an atomic level thickness (monolayer ratio: ≈ 70%) and have extremely low degree of oxidation and defects with the intrinsic structure preserved. In comparison with other fabrication techniques, this electrochemical method has several merits, such as scalable production, structural integrity with large size, affordable cost, solution-processability, and reproducibility. More importantly, exfoliated $NiPS_3$ flakes via cationic intercalation are not contaminated with oxygen groups. To the best of our knowledge, until now, this is the first MPT material that can be successfully exfoliated using an electrochemical technique without lithium ion intercalation. Due to fully exposed P and S atoms, the LSTL $NiPS_3$ flakes possess abundant active sites on the basal planes. By combining the experimental results with density functional theory (DFT) calculations, it is interesting to find that the S and P atoms on the basal planes of LSTL $NiPS_3$ are the active sites for the hydrogen evolution reaction (HER) and oxygen evolution reaction (OER), respectively.

The layered $NiPS_3$ crystallizes in the space group C2/m (No. 12) with a triclinic unit cell of a = 5.812 Å, b = 10.070 Å, c = 6.632 Å, and V = 371.2 $Å^3$. The model representing a lamella in both the normal direction and along the $NiPS_3$ layer stacking direction is illustrated in Figure S1 (Supporting Information). To acquire LSTL $NiPS_3$, bulk $NiPS_3$ materials with a large crystalline size is a prerequisite. Our prepared bulk $NiPS_3$ crystals by chemical vapor transport (CVT) method were highly crystalline with a closely stacked lamellar architecture with a maximum length of up to ≈1 cm (**Figure 1**a; Figures S2–S3, Supporting Information). The X-ray diffraction (XRD) pattern of the bulk $NiPS_3$ crystals exhibited an intense grain orientation along the c axis, and the peak positions matched well with the planes of the standard XRD data (JCPDS no. 01-78-0499) (Figure S4, Supporting Information), manifesting the layered crystal structure along the c axis and the pure phase of the $NiPS_3$ crystals.

Electrochemical exfoliation of bulk $NiPS_3$ crystals was performed in a two-electrode system (Figure 1b). An in-house electrochemical cell combined with optical microscopy (Figure S5, Supporting Information) was established to in situ monitor the intercalation and expansion process by implementing a constant voltage via chronoamperometry. The morphology changes in the $NiPS_3$ crystals were also monitored by ex situ scanning electron microscopy (SEM) (Figure 1f) and optical photographs (Figure S6, Supporting Information), and the corresponding mechanism are described in Figure 1e. First, bulk $NiPS_3$ crystals displayed tightly stratified architectures (Figure 1f; Figure S6a, Supporting Information). Then, tetra-*n*-butylammonium salts, which possess larger ionic diameters and could be used for exfoliating 2D materials, such as graphene, black phosphorus and phase-pure semiconducting nanosheets (MoS_2, WSe_2, Bi_2Se_3, $NbSe_2$, In_2Se_3, and Sb_2Te_3),[10] were selected as the salts for intercalation. When applying a constant negative bias (−3 V) to the working electrode for few seconds, the tetra-*n*-butylammonium tetrafluoroborate were intercalated into the interlamination of the bulk $NiPS_3$ crystals. These salts significantly weakened the van der Waals interactions between the layers and expanded the lattice to a greater extent (Figure 1f). Second, after applying a voltage for more time, the intercalated tetra-*n*-butylammonium salts were electrochemically decomposed into gaseous species, generating the driving force for gigantic and ultrafast volume expansion of the tightly stratified bulk $NiPS_3$ crystals together with edge wrinkling and roughening (Figure 1f; Movie S1, Supporting Information), followed by dissociation and dispersion into *N, N*-dimethylformamide (DMF) (Figure S6b–h, Supporting Information). The observed massive gas bubbles around the working electrode proved the decomposition of the intercalants. Finally, exfoliated $NiPS_3$ with unprecedentedly sizes and quality (Figure S7, Supporting Information) was detached from bulk $NiPS_3$ crystals by slight manual shaking, which supplied very weak hand-driven forces, forming LSTL $NiPS_3$ with preserved in-plane structural integrity. The in situ cyclic voltammograms (CV) measurement related to the intercalation and deintercalation of tetra-*n*-butylammonium salt was shown in Figure S8 (Supporting Information). DMF was selected as the nonaqueous electrolyte because of its low boiling point, high dispersion capability for the generated LSTL $NiPS_3$, much better than other commonly used solvent, such as propylene carbonate, dimethyl sulfoxide, and acetonitrile (Figures S9–S11, Supporting Information). After removal of the unexfoliated $NiPS_3$, the dispersion was filtered under vacuum and washed with a copious amount of DMF. The collected LSTL $NiPS_3$, after being redispersed in DMF exhibited the conspicuous Tyndall effect (Figure 1c). A high yield of ≈80% was determined by calculating the mass ratio of dried LSTL $NiPS_3$ and the starting bulk specimens. After electrochemical exfoliation, only the (001), (002), and (004) reflections of LSTL $NiPS_3$ was observed in XRD pattern, and the intensity was significantly smaller than that of bulk $NiPS_3$ crystals (Figure 1d). In addition, the peaks of the (130), (131), (221), (−133), (060), and (005) reflections disappeared for the exfoliated LSTL $NiPS_3$ (Figure S12, Supporting Information). These results pinpoint the successfully exfoliation of bulk $NiPS_3$ crystals into atomically thin $NiPS_3$ flakes.

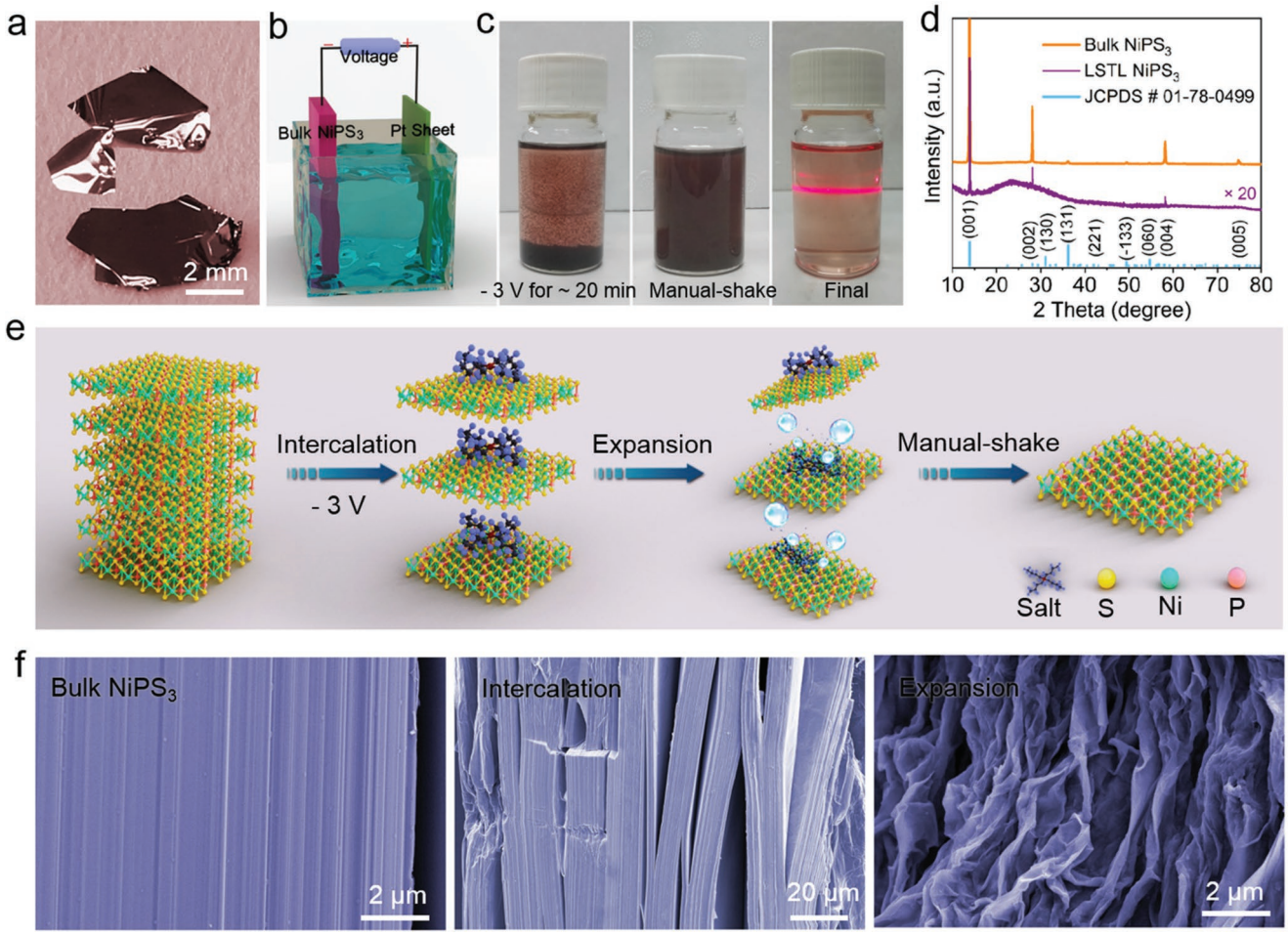

Figure 1. Mechanism of the electrochemical cathodic exfoliation. a) Photographs of the single crystal bulk $NiPS_3$ specimens. b) Schematic illustration of the experimental setup for electrochemical exfoliation. c) Images of (left) expanded $NiPS_3$ in DMF after electrochemical charging at −3 V for ≈20 min; (center) dispersion of expanded $NiPS_3$ via manual shaking; and (right) final LSTL $NiPS_3$ dispersion exhibiting the Tyndall effect. d) XRD patterns of the bulk and LSTL $NiPS_3$ samples with a standard JCPDS pattern (01-78-0499). The wide peak ≈20–30° was assigned to the silicon substrate. e) Mechanism illustration of electrochemically exfoliating bulk $NiPS_3$ crystals in tetra-*n*-butylammonium salts solution. f) Ex situ SEM images of $NiPS_3$ after applying a bias voltage of −3 V for 0, 30, and 60 s in tetra-*n*-butylammonium salts solution.

To study the morphology and structure of LSTL $NiPS_3$, optical microscopy, transmission electron microscopy (TEM), and atomic force microscope (AFM) were performed. **Figure 2**a depicts the optical microscope image of high-coverage LSTL $NiPS_3$. The low-magnification optical microscope and TEM images showed that ample intertangling and crinkles were on the surface of LSTL $NiPS_3$ (Figure 2b,c). Subsequently, the atomic lattice of LSTL $NiPS_3$ was analyzed via high resolution TEM (HRTEM). The distance between adjacent lattice fringes was measured to be 2.87 Å, which exactly matched the theoretical value (Figure 2d). High-angle annular dark field-scan TEM (HAADF- STEM) of the (131) plane was further conducted, and the results are shown in Figure 2e. A homogeneous and almost defect-free structure was verified across the entire single crystal domain. In addition, the pattern was consistent with the image simulation along the *c* axis. The pattern revealed three sets of lattice fringes with spacings of 1.62, 1.68, and 1.62 Å, which corresponds well to the (330), (060), (330) planes of LSTL $NiPS_3$, respectively. All the consequences highlighted the atomic structure of LSTL $NiPS_3$ with intact phase structure and excellent crystalline quality. Furthermore, the TEM-electron energy loss spectrometer (EELS) mapping revealed a uniform distribution of Ni, P, and S elements over the entire exfoliated flake (Figure S13, Supporting Information). To ascertain the accurate thickness of LSTL $NiPS_3$, representative AFM images of LSTL $NiPS_3$ were exhibited in Figure 2f. The topographic height was ≈0.92 nm, which can be assigned to a monolayer of $NiPS_3$. The statistical analysis based on large-area AFM measurements (Figure 2g) indicated that the monolayer ratio of LSTL $NiPS_3$ was ≈70% (Figure 2h; Figure S14, Supporting Information). The parameter comparison of LSTL $NiPS_3$ and other reported $NiPS_3$ specimens is provided in Figure 2i and Table S1 in the Supporting Information. To the best of our knowledge, the electrochemical exfoliation reported here is the highest efficiency pathway for the preparation of large quantities of high-quality $NiPS_3$ with a large area and atomical thickness.[2,4–6,9]

Subsequently, a structural comparison between bulk $NiPS_3$ and LSTL $NiPS_3$ was implemented. An X-ray photoelectron

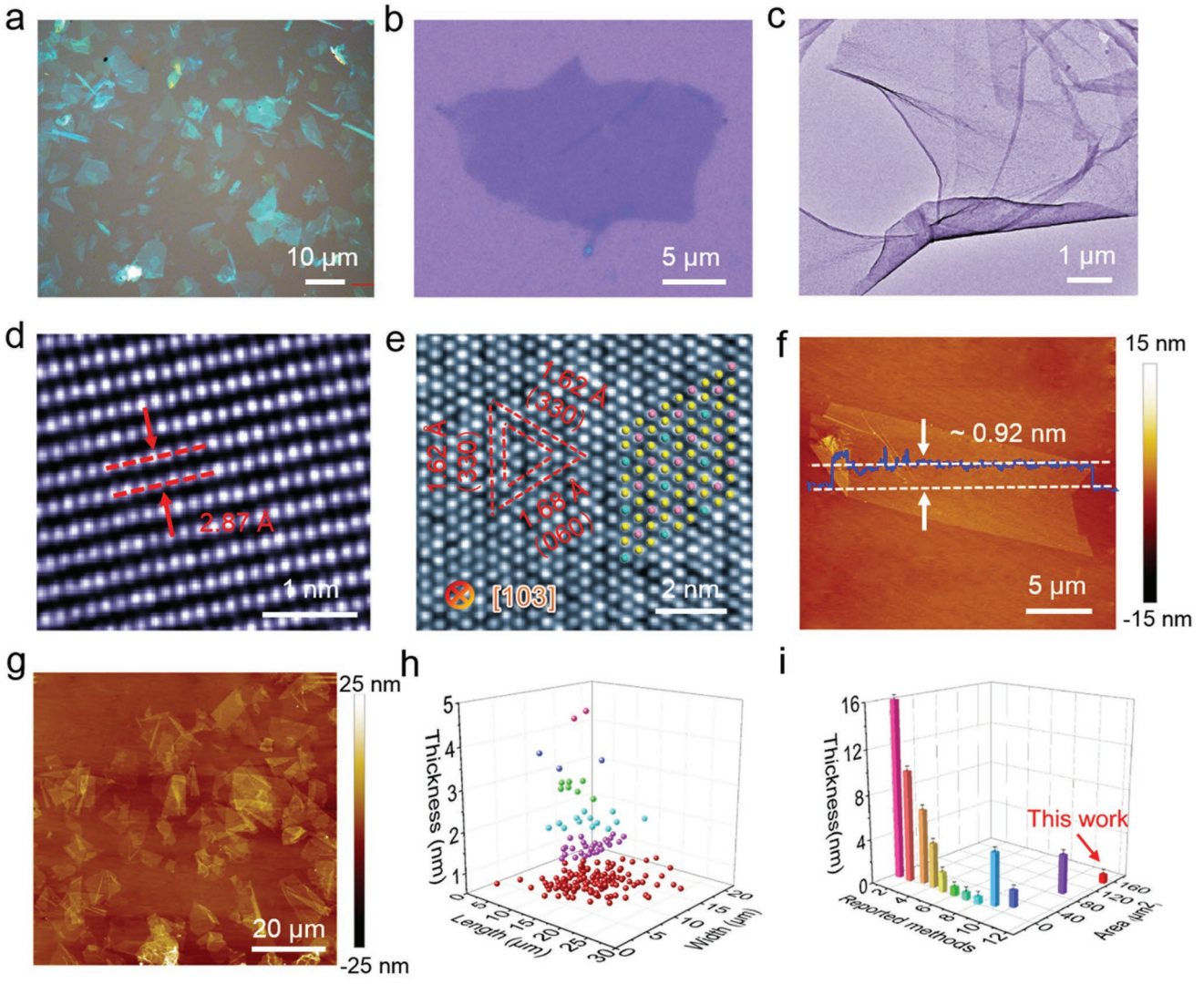

Figure 2. Morphological and structural characterization of LSTL $NiPS_3$. a) Typical optical microscope image of high-coverage LSTL $NiPS_3$ on mica substrate. b) Representative optical microscope image of single LSTL $NiPS_3$ on SiO_2/Si substrate. c) TEM, d) HRTEM, e) HAADF-TEM images of LSTL $NiPS_3$. f) AFM image of large-sized and monolayer $NiPS_3$ on SiO_2/Si substrate. g) High-coverage AFM image of LSTL $NiPS_3$ on mica substrate. h) Statistical analysis of length, width, and thickness distribution of LSTL $NiPS_3$. The total number of LSTL $NiPS_3$ for statistics was about 200. i) Parameter comparison of LSTL $NiPS_3$ and other previously reported $NiPS_3$. "1-11" stands for published paper.[2,5,6]

spectroscopy (XPS) spectrum revealed distinct signals of Ni, P, and S in LSTL $NiPS_3$ (Figure S15, Supporting Information). The atomic percentages of Ni (15.8 at%), P (25.1 at%), and S (59.1 at%) were estimated. The resolved Ni 2p spectrum illuminated the spin–orbit doublets for the $2p_{3/2}$ (854.43 eV) levels of the typical Ni^{2+} species along with three satellite peaks at 856.5, 859.5, and 864.4 eV (**Figure 3**a).[2b] In the P 2p spectrum (Figure 3b), two peaks at 131.95 and 132.79 eV of covalent P–S in the PS_3 units were ascribed to P $2p_{3/2}$ and P $2p_{1/2}$, respectively.[5c] The S 2p spectrum also displayed double peaks at 162.46 and 163.64 eV, attributed to Ni–S and P–S, respectively (Figure 3c).[5c] Notably the XPS results revealed that LSTL $NiPS_3$ obtained by electrochemically cathodic exfoliation only exhibited characteristic peaks of P $2p_{3/2}$, P $2p_{1/2}$, S $2p_{3/2}$, and S $2p_{1/2}$. The peaks centered at ≈134.5 eV and ≈167.8 eV associated with oxidized P and S were not observed,[1a,11,12] suggesting the negligible oxidation degree of LSTL $NiPS_3$. In contrast, traditional exfoliation methods always suffered from the production of 2D materials with an unwanted high oxidation degree.[11,12] The Ni 2p, P 2p, and S 2p peaks also display a slight redshift in the binding energy compared to those of the bulk crystals (Figure S16, Supporting Information), probably originating from the thickness change in $NiPS_3$ during electrochemical exfoliation (Figure S17, Supporting Information).

The variations in the coordination environment for Ni atoms were probed by X-ray absorption fine structure (XAFS) analysis. The Ni K-edge X ray absorption near edge structure (XANES) (Figure 3d) and Fourier transformed (FT) $k^3\chi(k)$ function extended X-ray absorption fine structure (EXAFS) spectra (Figure 3e) and also their corresponding $k^3\chi(k)$ oscillation curves (Figure S18, Supporting Information) of the obtained LSTL $NiPS_3$ exhibited similar but different features compared with

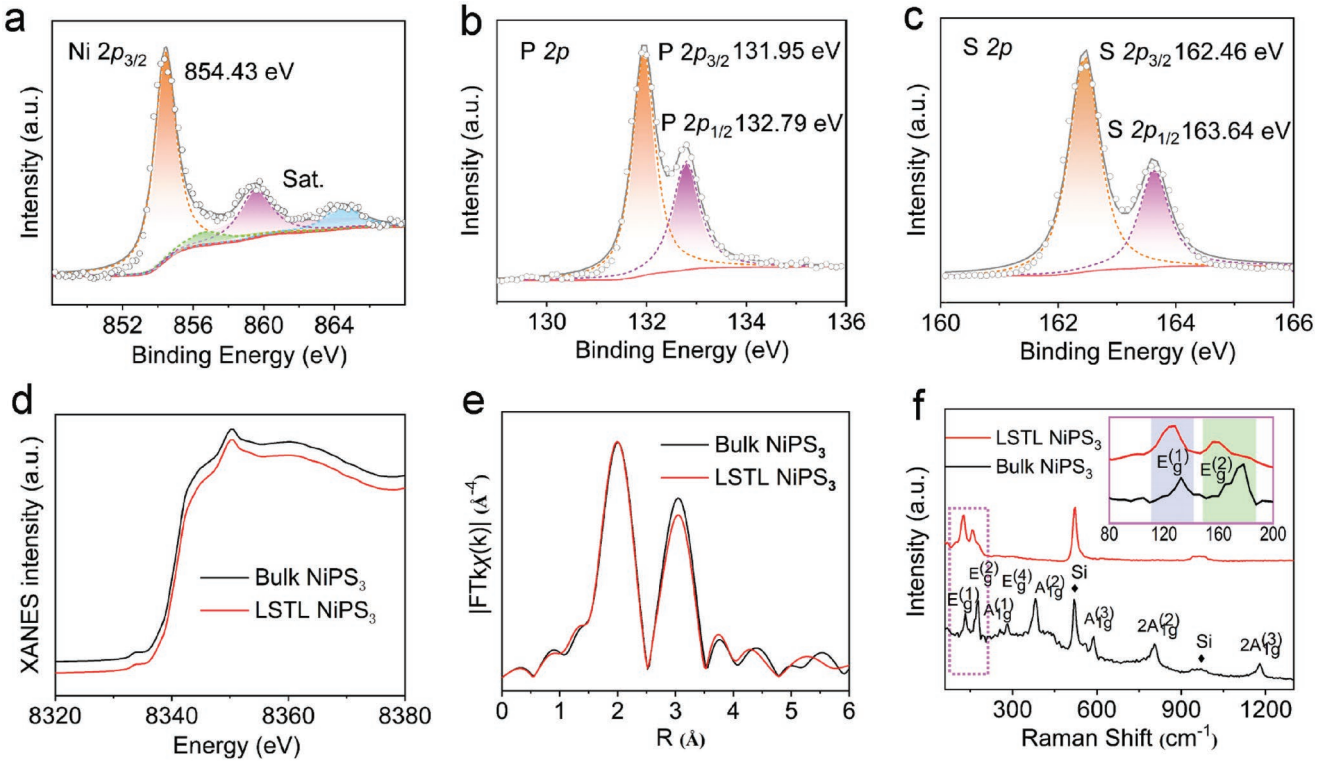

Figure 3. Structure comparison between bulk $NiPS_3$ crystals and LSTL $NiPS_3$. High-resolution XPS spectra of the a) Ni 2p, b) P 2p, and c) S 2p regions of electrochemically exfoliated LSTL $NiPS_3$. Ni-K edge d) XANES, e) FT-EXAFS spectra of the bulk $NiPS_3$ crystals and LSTL $NiPS_3$. f) Raman spectra of the bulk $NiPS_3$ crystals and LSTL $NiPS_3$ in the range from 100 to 1250 cm^{-1}.

bulk $NiPS_3$ crystals. The Ni K-edge XANES spectra presented a Ni oxidation state (Figure 3d). The results for the energy of the absorption edge combined with the intensity of the white line demonstrated that the valence of Ni in LSTL $NiPS_3$ was higher than that in bulk structure, which indicated a more abundant coordinate environment for LSTL $NiPS_3$.[13] The peak positions that corresponds to the Ni–S coordination for $NiPS_3$ exhibited the same radial distance (2.00 Å) as that of bulk structure (Figure 3e). Moreover, the second coordination shell peak intensity of LSTL $NiPS_3$ decreased significantly (11%) compared to that of bulk crystals, demonstrating the obvious structural distortion and the dimension reduction of $NiPS_3$ crystals.[7c] A curve fitting was also conducted to obtain the detailed structure parameters (Table S2, Supporting Information). The Ni—S bond in LSTL $NiPS_3$ showed supersaturated coordination, giving a higher coordination number (CN) of 5.6 (Ni–S) than that of the bulk crystals (CN = 5.4 for the Ni–S). Moreover, the fitted bond length results suggested that there was an obvious structural distortion in LSTL $NiPS_3$ because of the increasing Ni—S bond length. The supersaturated coordination and structural distortion of LSTL $NiPS_3$ likely resulted from the highly exposed supersaturated-coordinated edge sites,[14] further clarifying the atomic thin 2D character for LSTL $NiPS_3$.

Raman spectroscopy measurements of bulk $NiPS_3$ crystals and LSTL $NiPS_3$ excited by 532 nm laser on a SiO_2/Si substrate were also systematically performed. As displayed in Figure 3f, the three in-plane E_g modes, three out-of-plane A_g modes, and two second-order A_g modes were detected. $A_{1g}^{(1)}$ was dominated by the in-plane motions of the sulfur planes, while $A_{1g}^{(2)}$ and $A_{1g}^{(3)}$ were assigned to the vertical components of their sulfur plane vibrations. $E_{1g}^{(1)}$ was attributed to Ni^{2+} metal ions, and the 434 cm^{-1} peak was attributed to the P—P bond vibrational mode.[4,5b,6] For LSTL $NiPS_3$, only $E_g^{(1)}$ and $E_g^{(2)}$ were detected, which was ascribed to a weakening of the interlayer interaction with a reduction in flake thickness.[4] Moreover, compared with bulk $NiPS_3$, the Raman modes of LSTL $NiPS_3$ revealed a distinct shift toward lower wavenumbers (inset of Figure 3f), which was attributed to the phonon confinement effect because of the ultrathin thickness.[5c,6]

Recently, numerous outstanding 2D electrocatalysts have been established for the half reaction of water splitting. For example, transition metal sulfides (e.g., NiS_x, MoS_2) and phosphides (e.g., Ni_2P) have shown promising HER and OER performance, whereas S-atoms and P-atoms are often suggested as the active sites for HER and OER, respectively.[15–18] However, most 2D catalytic materials have only a single-functional activity site that can only be used for a single half reaction. Thus, it remains an enormous challenge to exploit brand-new 2D materials with multifunctional activity sites to realize overall water splitting. Herein, LSTL $NiPS_3$ with high crystallinity and pure phase structure produced by electrochemical exfoliation perfectly combine the fully exposed S and P atoms in one 2D material, which offers an ideal model to exploit their inherent reactivity for overall water splitting.

In the atomic structure of $NiPS_3$, Ni atoms on the basal planes immobilized the $[P_2S_6]^{4-}$ framework and were

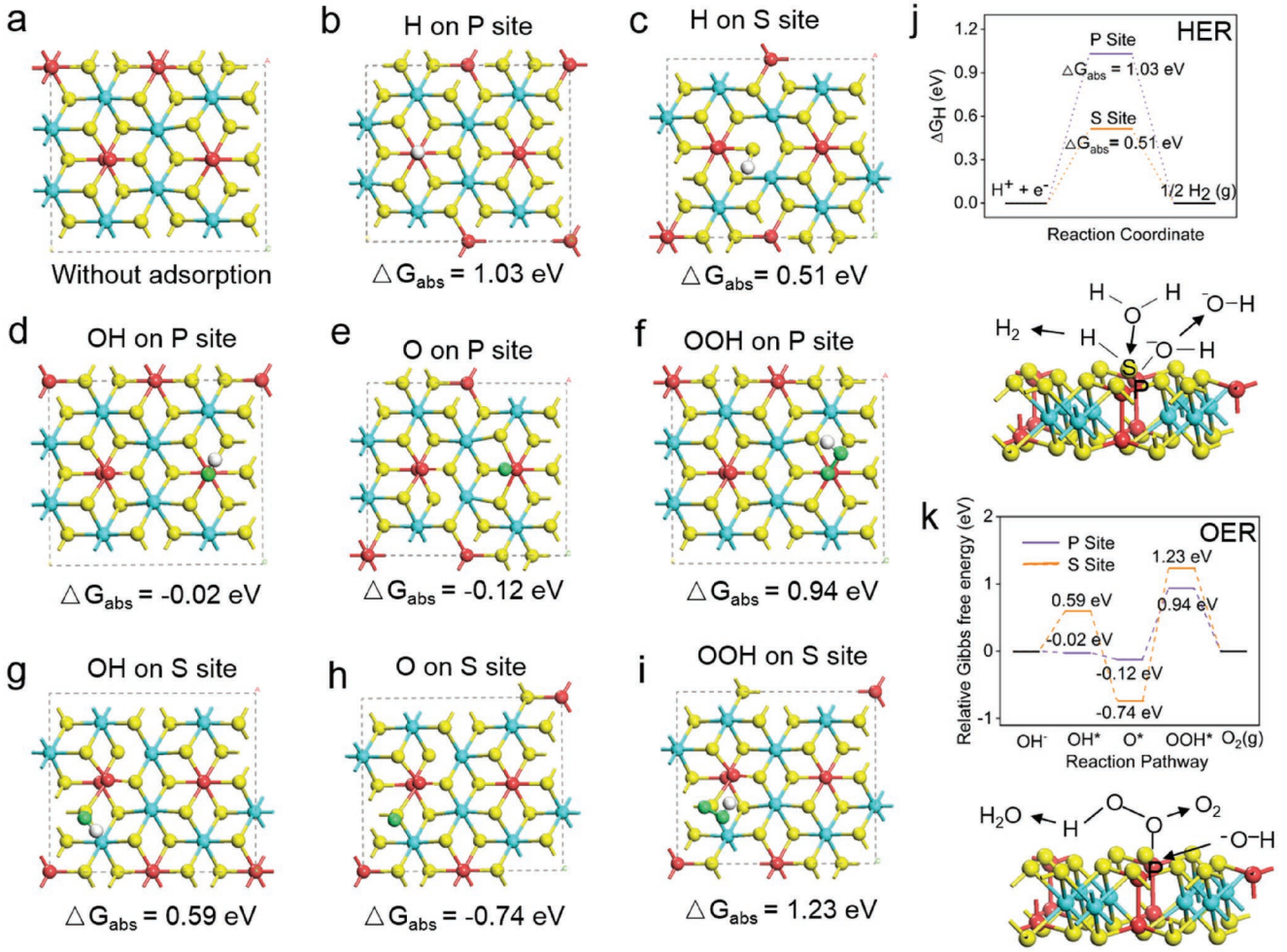

Figure 4. Chemisorption models and calculated free energy. a–i) Chemisorption models of the H and OH intermediates on the P and S sites in $NiPS_3$ for the HER and OER respectively. The corresponding adsorbed configurations in the $NiPS_3$ (100) direction were shown in Figure S20 (Supporting Information). i–k) Calculated free energy diagram on the $NiPS_3$ (001) surfaces for the HER and OER at equilibrium (applied potential $U = 0$) with the adsorbed configurations shown in (a–i), and the proposed mechanisms of the dissociation of H_2O, OH on LSTL $NiPS_3$. The blue balls represent Ni atoms, red for P, yellow for S, white for H, and cyan for O.

sandwiched by the S layers;[1c] thus, they could not be exposed and serve as active sites, which is similar to MoS_2.[16,18,19] To accurately clarify the effect of P and S atoms on the OER and HER, DFT was utilized to calculate the chemisorption free energies of hydrogen (ΔG_H) and hydroxide (ΔG_{OH}). **Figure 4**a–c,j show that ΔG_H value was 1.03 eV for the P sites and 0.51 eV for the S site, respectively. Distinctly, the adsorption of H atoms on the S sites was much more favorable, namely, the S atoms on the basal planes of LSTL $NiPS_3$ were the active sites of HER. Considering water dissociation process in alkaline solution, we further performed transition state calculation related to the water dissociation step. The energy barrier in-between was located via searching for transition states by climbing image-nudged-elastic band method. As shown in Figure S19 (Supporting Information), when the kinetics of water dissociation from the Volmer step was considered, the S sites in 2D $NiPS_3$ exhibited a significant water dissociation barrier (E_a = 1.48 eV), substantively lower than that on P sites in 2D $NiPS_3$ (E_b = 3.41 eV). Therefore, from the kinetic viewpoint, the S atoms on the basal planes of LSTL $NiPS_3$ were the active sites of HER, which was consistent with the result in Figure 4j. Figure 4d–i,k also display the calculated free energy along the OER pathway for the P and S sites. The adsorption of OH^- onto the S atom needs an energy of 0.59 eV, which is energy unfavorable and prohibits continuing the OER. Furthermore, the conversion of O* to OOH*, which needs the largest uphill energy, is the rate-determining step for both P (1.06 eV, O* → OOH*) and S (1.97 eV, O* → OOH*). Obviously, P atoms on the basal planes possess the lower reaction energy barrier than S atoms, indicating its great potential as active sites for OER.

Due to abundant fully exposed multifunctional active sites on the basal planes (Figure S21, Supporting Information), a superhigh electrochemically active surface area (Figure S22, Supporting Information), and improved mass/electron transport (Figure S23, Supporting Information), LSTL $NiPS_3$ could be employed as bifunctional electrocatalysts for water splitting. Thus, LSTL $NiPS_3$ immobilized on commercial nickel foam

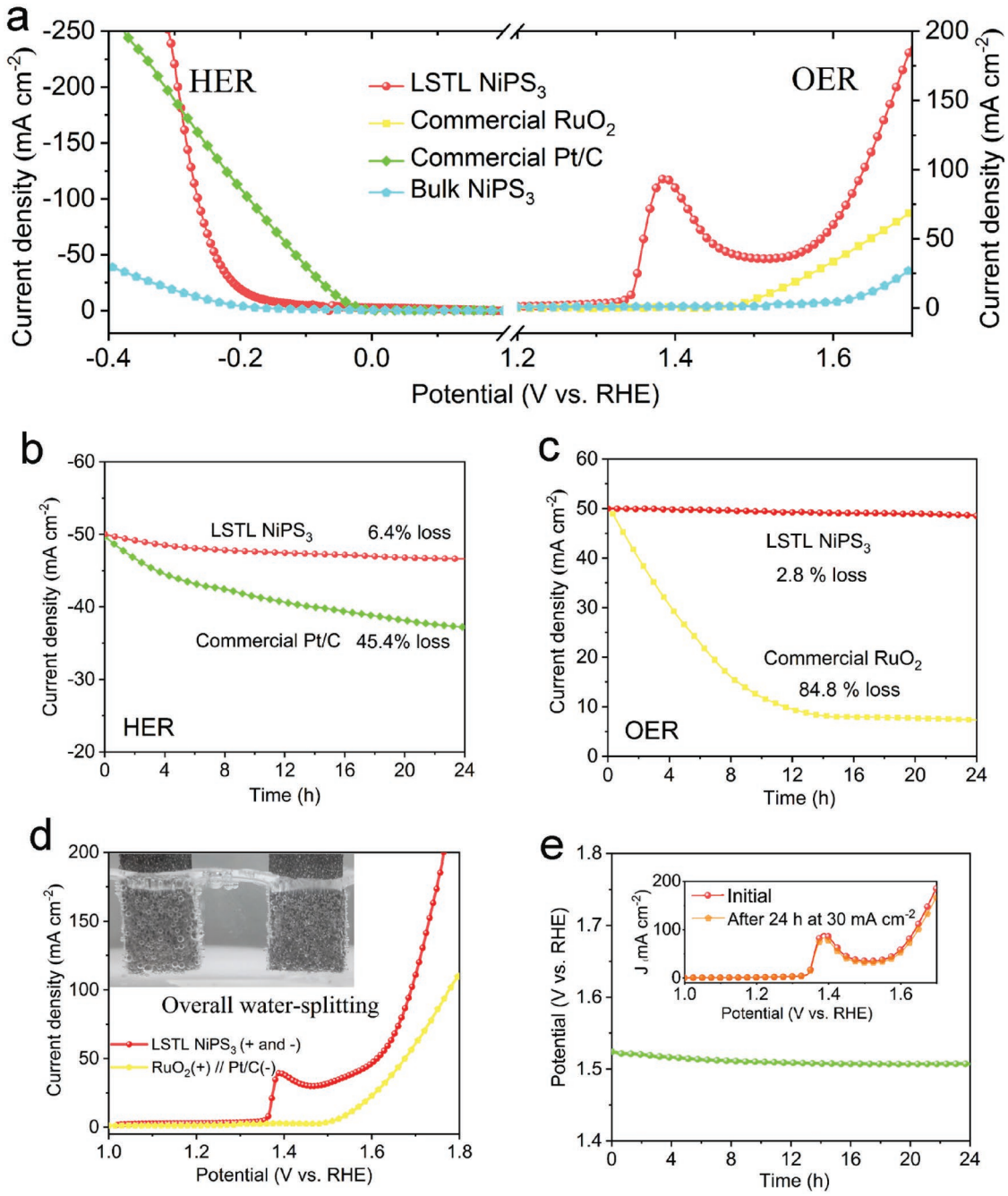

Figure 5. HER, OER, and overall water-splitting performance of LSTL $NiPS_3$. a) Steady-state LSV curves at a scan rate of 5 mV s^{-1}. b,c) Chronoamperometry curves of these electrodes at a high current density of 50 mA cm^{-2}. d) LSV curves of LSTL $NiPS_3$, and RuO_2 (+) // Pt/C (–) for overall water splitting in a two-electrode configuration. Inset: photograph of bubble overflow on LSTL $NiPS_3$ during overall water splitting. e) Chronopotentiometry curves of LSTL $NiPS_3$ under a current density of 30 mA cm^{-2}. Inset: LSV curves of LSTL $NiPS_3$ before and after chronopotentiometry measurement.

served as the working electrode to catalyze the HER and OER (Figure S24, Supporting Information). Bulk $NiPS_3$ crystals, commercial Pt/C and RuO_2 catalysts were also investigated for comparison. As illustrated in the left panel of **Figure 5**a, LSTL $NiPS_3$ displayed high activity for the HER, and the onset potential was ≈100 mV, much lower than that of bulk $NiPS_3$ (200 mV). To realize a current density of 10 mA cm^{-2}, an overpotential of only 158 mV was required for LSTL $NiPS_3$, but 250 mV was required for bulk $NiPS_3$ crystals. In addition, when the overpotential exceeded 290 mV, the HER activity of LSTL $NiPS_3$ was observably superior to commercial Pt/C. Such performance transcended many of the previously reported nonprecious metal HER electrocatalysts (Table S3, Supporting Information). Furthermore, the catalytic kinetics were assessed from the Tafel plots.[20–22] The Tafel slope value of LSTL $NiPS_3$ was ≈95 mV dec^{-1}, which was lower than the bulk $NiPS_3$

crystals (159 mV dec^{-1}) (Figure S25, Supporting Information), signifying its superior HER rate.

Subsequently, the OER performance of these materials were studied. As revealed in the linear sweep voltammetry (LSV) curves in the right panel of Figure 5a, the oxidation peak associated with the transition from Ni^{2+} to Ni^{3+} occurred between 1.35 and 1.45 V.[13] Therefore, a backward CV scan was employed to estimate the OER performance of LSTL $NiPS_3$. As displayed in Figure S26 (Supporting Information), LSTL $NiPS_3$ exhibited an extraordinarily low onset potential (1.45 V), which was significantly lower than the bulk $NiPS_3$ crystals (1.60 V) and even superior to commercial RuO_2 (1.48 V). To realize a current density of 10 mA cm^{-2}, LSTL $NiPS_3$ required an overpotential of only 300 mV, outperforming bulk $NiPS_3$ crystals and commercial RuO_2. The Tafel slope of LSTL $NiPS_3$ was 88 mV dec^{-1}, which was also obviously lower than that of the bulk $NiPS_3$ crystal (152 mV dec^{-1}, Figure S25, Supporting Information). This excellent OER performance of LSTL $NiPS_3$ was superior to that of many transition metals and even some noble-metal electrocatalysts (Table S4, Supporting Information).

Long-term stability is another significant parameter for both the electrocatalytic HER and OER. As depicted in Figure 5b,c, a current density of 50 mA cm^{-2} for the HER (overpotential: 239 mV) and OER (overpotential: 350 mV) could be maintained for more than 24 h with a trivial current decline of 6.4% and 2.8%, respectively. However, both commercial Pt/C and RuO_2 catalysts with the same mass loading were unstable under the same test conditions, and the current densities of 50 mA cm^{-2} showed a significant decrease of merely 54.6% and 15.2% maintaining, respectively. The decline in the stability of RuO_2 was probably because of the oxidation of RuO_2 to water-soluble RuO_4^{2-} or other solvated Ru^{VI} ions under alkaline conditions.[23] The decrease in Pt/C stability was mainly attributed to Pt particles largely peeling off the support, caused by the generated H_2 bubbles during long reaction times.[24] The morphology and chemical composition of the LSTL $NiPS_3$ after the HER and OER stability tests was displayed in Figures S27–S28 (Supporting Information).

Inspired by the remarkable HER and OER performances, we assembled a water electrolyzer in 1.0 M KOH by applying LSTL $NiPS_3$ as both the anode and cathode electrode for overall water splitting. As indicated in Figure 5d, the overall water splitting performance of LSTL $NiPS_3$ was much better than the RuO_2–Pt/C couple. To deliver a current density of 10 mA cm^{-2}, ≈1.56 V was required, that is, a combined overpotential of ≈330 mV for electrochemical overall water splitting. The electrocatalytic overall water splitting activity at 30 mA cm^{-2} was also monitored (Movie S2, Supporting Information). The results revealed that massive H_2 and O_2 bubbles were rapidly generated on both LSTL $NiPS_3$ electrodes. More importantly, LSTL $NiPS_3$ exhibited outstanding stability with an insignificant decline in a 24 h galvanostatic electrolysis at 30 mA cm^{-2} (Figure 5e). The comparison of the overall water splitting performance in a 1.0 M KOH solution for LSTL $NiPS_3$ with other bifunctional electrocatalysts is displayed in Table S5 (Supporting Information), which further highlights its robust catalytic performance.

In summary, we have successfully demonstrated that large-size and atomically thin $NiPS_3$ flakes with high crystallinity and pure phase structure can be prepared by a sonication-free and fast (in minutes) electrochemical cathodic exfoliation approach with a high yield. With the help of tetra-*n*-butylammonium salt with large ionic diameter and gas releasing nature, atomically thin monolayer or few-layer $NiPS_3$ can be obtained by slight manual shaking after the electrochemical intercalation. Due to the fully exposed P and S catalytic active site without contamination of oxygen groups, the exfoliated $NiPS_3$ flakes possess ultrahigh electrochemically active surface area and extremely low reaction resistance, which deliver a robust HER, OER and enable efficient overall water-splitting performance. The successful electrochemical cathodic exfoliation of $NiPS_3$ provides the possibility for the scalable preparation of other MPT and 2D materials and facilitates the development of 2D-based applications.

Experimental Section

Chemicals: Red phosphorus powder (99.999%), tetra-*n*-butylammonium tetrafluoroborate (99%), RuO_2 (99.95% metal basis), and Nafion (0.5 wt%) were purchased from Alfa Aesar. Sulfur powder (99.999%) and nickel powders (99.99%) was purchased from Adamas-beta. DMF (99%) and KOH were purchased from Macklin. The commercial Pt/C (20 wt%) catalysts were obtained from Johnson Matttey (Shanghai, China). Water was purified through a Millipore system.

Synthesis of Bulk $NiPS_3$ Crystals: Bulk $NiPS_3$ crystals were prepared by the CVT method. High-purity nickel, phosphorus and sulfur powders (total mass: ≈ 2 g) with a stoichiometric mole ratio (1:1:3) were fully mixed and grinded in a glove box. Then, powders were sealed in an evacuated quartz tube (length: 25 cm; external diameter: 13 mm; wall thickness: 1 mm) under a vacuum of 10^{-5} Pa using an oxygen/hydrogen welding torch by Partulab device (MRVS-1002, Partulab Technologies, China). Next, the sealed tube was placed in a two-zone furnace. Then, the temperature in the reaction and growth zone were programmed to 700 °C and 650 °C with a heating rate of 1 °C min^{-1}, and the corresponding temperature was maintained for 7 days to generate a temperature gradient for the growth of the bulk crystals. Finally, the two-zone furnace was cooled naturally to ambient temperature, and the bulk $NiPS_3$ crystals were collected.

Electrochemical Exfoliation of Bulk $NiPS_3$ Crystals: The electrochemical exfoliation of bulk $NiPS_3$ crystals was performed by using an electrochemical workstation (CHI 760E, Shanghai Chenhua Instrument Factory, China) consisting of a two-electrode system. The obtained bulk $NiPS_3$ crystals were clamped to a Pt clip and were employed as the working electrode. A Pt sheet (length: 10 mm; width:10 mm) electrode was utilized as the counter electrode and was installed ≈1.5 cm away from the bulk $NiPS_3$ crystals. A DMF solution (60 mL) consisting of 0.05 M tetra-*n*-butylammonium tetrafluoroborate was used as the electrolyte.

The electrochemical exfoliation of bulk $NiPS_3$ crystals to LSTL $NiPS_3$ was performed by executing a static bias of −3 V on the working electrode. After the exfoliation process was accomplished, the obtained suspension was manually shaken for ≈20 s, and then the dispersion was centrifuged to precipitate unexfoliated $NiPS_3$. The top part of the dispersion was filtered through a nylon membrane filter (Agela Technologies, 47 mm, 0.45 μm) and washed with plenty of DMF by vacuum filtration to remove the residual tetra-*n*-butylammonium salts. Finally, the collected LSTL $NiPS_3$ was redispersed in DMF for characterization and application.

Electrode Preparation: Nickel foam served as the 3D scaffold, which was sonicated and washed in acetone, ethanol, 0.5 M HCl solution and water. Subsequently, the 2 mL LSTL $NiPS_3$ dispersion (2 mg mL^{-1}) containing a 200 μL Nafion (0.5 wt%) aqueous solution was uniformly dispersed onto the dried nickel foam (1 × 2 cm^2) and then dried in a vacuum drying oven. Thus, the loading weight of LSTL $NiPS_3$ on the nickel foam was ≈1.0 mg cm^{-2}. For comparison, commercial Pt/C and RuO_2 catalysts were loaded on nickel foam with the same loading

(1.0 mg cm^{-2}) and acted as both the cathode and anode electrode, respectively.

Electrochemical Tests: The electrochemical HER and OER activities were investigated in a three-electrode system equipped with a proton exchange membrane (Nafon-117 membrane). A saturated Ag/AgCl electrode in 3.0 M KCl solution and a Pt sheet served as the reference and counter electrodes, respectively. All the potentials were converted to the reversible hydrogen electrode (RHE) scale via the Nernst Equation (1)

$$E_{RHE} = E_{SHE} + 0.0591 \times pH = E_{APPL} + \phi_{Ag/AgCl} + 0.0591 \times pH \quad (1)$$

in which, E_{SHE} is the potential versus standard hydrogen electrode (SHE) potential, E_{Appl} is the applied potential versus Ag/AgCl reference, and $\phi_{Ag/AgCl}$ is the electrode potential of the KCl-saturated Ag/AgCl reference electrode (0.198 V vs SHE). Unless otherwise noted, all potentials used refer to the RHE via calibration. All current densities were normalized using the geometrical area of the nickel foam immersed in solution (2 cm^{-2}).

The HER and OER performances were investigated in 1.0 M KOH by the LSV method within the range of –0.5 to 0.5 V and 1.0–1.8 V, corrected by iR-compensation (80%) for the ohmic potential drop losses. For the OER, a flow of O_2 was employed to ensure the O_2/H_2O equilibrium at 1.23 V. For the HER, a flow of Ar was used to purge the electrolyte. The overpotentials (η) at 10 mA cm^{-2} were ascertained based on the Equation (2), and the Tafel slope (b) was calculated according to Tafel Equation (3)

$$\eta = E(\text{versusRHE}) - 1.23 \quad (2)$$

$$\eta = a + b\log|J| \quad (3)$$

Chronopotentiometry and chronoamperometry measurements were performed to evaluate the stability. Electrochemical impedance spectra (EIS) were recorded at 1.51 V from 100 kHz to 0.01 Hz with amplitude 5 mV in O_2-saturated 1.0 M KOH solution. The electrochemically active surface areas of bulk $NiPS_3$ and LSTL $NiPS_3$ were estimated by using CV in an O_2-saturated 1.0 M KOH solution at different scan rates (20, 40, 60, 80, and 100 mV s^{-1}).

Material Characterization: The $NiPS_3$ suspension prepared by electrochemical exfoliation was dispersed onto a superthin carbon-coated porous copper grid for TEM, a frosted glass for XRD, clean silicon substrates for SEM, optical microscopy and XPS, a clean SiO_2/Si substrate for Raman characterization, a mica substrate for AFM. XRD (Ultima IV, Rigaku Corporation, Japan) measurements were performed with Cu-Kα radiation as the X-ray source (λ = 1.5418 Å). The TEM, HRTEM, and HAADF-STEM images were obtained by employing probe Cs-corrected TEM equipment (FEI Titan ChemiSTEM, USA). Energy dispersive X-ray spectroscopy was utilized to characterize the elemental mapping of LSTL $NiPS_3$. SEM images were acquired by employing a field emission SEM (Zeiss SUPRA 55, Carl Zeiss, Germany). AFM images were acquired by employing a Bruker Dimension FastScan Atomic Force Microscope (Bruker L01F4C8, USA) in tapping mode in air. Optical imaging of bulk $NiPS_3$ and LSTL $NiPS_3$ on the SiO_2/Si and mica substrate was conducted using an optical microscope (Nikon ECLIPSE LV100ND, Japan). Raman spectra and mapping were recorded at room temperature using a WITec (Alpha 300R, Germany) Raman Microscope with laser excitation at 532 nm. XPS measurements were obtained using an ESCALAB 250Xi (Thermo Fisher, UK) X-ray photoelectron spectroscopy instrument. The sample analysis chamber pressure was $\approx 5 \times 10^{-10}$ mbar during the spectrum acquisition. X-ray absorption spectra were collected at Shanghai Synchrotron Radiation Facility (SSRF) on beamline BL14W1. The storage ring was operated at electron energy of 2.5 GeV with a beam current of 250 mA. A Si (111) double-crystal monochromatic was applied. The beam size used at the sample position was $\approx 900 \times 300$ μm^2. All the data were collected at ambient temperature applied in the transmission mode. More details are shown in Note S4 in the Supporting Information.

Computational Details and Models: DFT calculations were carried out using the plane-wave technique with exchange-correlation interactions modeled by GGA-PBE functional,[25] as implemented in the Vienna ab initio simulation package (VASP).[26] The ion–electron interactions were described by the projector augmented plane wave approach and the cutoff energy was set to 500 eV.[27] Structural optimizations were performed by minimizing the forces on all the atoms to below 0.02 eV·$Å^{-1}$ and minimizing the energy to below 10^{-5} eV. The Monkhorst–Pack method was adopted to sample the k-space with an $8 \times 4 \times 8$ mesh for the bulk and a $4 \times 4 \times 1$ mesh for the surface of the $NiPS_3$ system. To describe the strongly correlated d electrons of a Ni atom, the GGA + U (U = 4 eV) scheme introduced by Dudarev et al was employed.[28,29] The van der Waals correction was included using Becke-Jonson damping with function parameters of the D3 method by Grimme et al.[30] To explore the catalytical performance of $NiPS_3$, a (2×1) slab of the (001) surface was constructed with a vacuum layer of 15 Å to avoid the interaction between neighboring images. Additionally, the dipole corrections were employed in all slabs calculations. All the atoms in the slab were relaxed during the geometrical optimization process. The free energy analyzing method developed by Nørskov et al was used to predict the reaction activity.[31] In the end, the Equation (4) was adopted to evaluate the adsorption free energy of H on different sites of the $NiPS_3$ surface, where the ΔE_{H^*} is the adsorption energy of a H atom

$$\Delta G_{H^*} = \Delta E_{H^*} + 0.24\text{eV} \quad (4)$$

Supporting Information

Supporting Information is available from the Wiley Online Library or from the author.

Acknowledgements

X.L. and Y.F. contributed equally to this work. The authors acknowledge the support from the National Natural Science Foundation of China (Nos. 61875139, 91433107, 51502174, 91645102, and 51702219), Research Foundation of China Postdoctoral Science (2018M630976), the National Key Research & Development Program (No. 2016YFA0201900), Guangdong Special Support Program, Shenzhen Peacock Plan (Grant Nos. 827-000113, KQJSCX20170727100802505, and KQTD2016053112042971), the Educational Commission of Guangdong Province (2016KTSCX126), Shenzhen Nanshan District Pilotage Team Program (LHTD20170006), Science and Technology Project of Shenzhen (ZDSYS201707271014468), and Australian Research Council (ARC, FT150100450, IH150100006, and CE170100039).

Conflict of Interest

The authors declare no conflict of interest.

Keywords

2D materials, bifunctional, electrochemical exfoliation, $NiPS_3$, overall water splitting

Received: May 13, 2019
Published online: June 7, 2019

[1] a) X. Zhang, Z. Luo, P. Yu, Y. Cai, Y. Du, D. Wu, S. Gao, C. Tan, Z. Li, M. Ren, T. Osipowicz, S. Chen, Z. Jiang, J. Li, Y. Huang, J. Yang, Y. Chen, C. Y. Ang, Y. Zhao, P. Wang, L. Song, X. Wu, Z. Liu, A. Borgna, H. Zhang, *Nat. Catal.* **2018**, *1*, 460; b) X. Li, X. Wu, J. Yang, *J. Am. Chem. Soc.* **2014**, *136*, 11065; c) M. A. Susner,

M. Chyasnavichyus, M. A. McGuire, P. Ganesh, P. Maksymovych, *Adv. Mater.* **2017**, *29*, 1602852; d) Z. Cheng, T. A. Shifa, F. Wang, Y. Gao, P. He, K. Zhang, C. Jiang, Q. Liu, J. He, *Adv. Mater.* **2018**, *30*, 1707433.

[2] a) Q. Liang, Y. Zheng, C. Du, Y. Luo, J. Zhang, B. Li, Y. Zong, Q. Yan, *Small Methods* **2017**, *1*, 1700304; b) R. Dangol, Z. Dai, A. Chaturvedi, Y. Zheng, Y. Zhang, K. N. Dinh, B. Li, Y. Zong, Q. Yan, *Nanoscale* **2018**, *10*, 4890.

[3] S. Y. Kim, T. Y. Kim, L. J. Sandilands, S. Sinn, M.-C. Lee, J. Son, S. Lee, K.-Y. Choi, W. Kim, B.-G. Park, C. Jeon, H.-D. Kim, C.-H. Park, J.-G. Park, S. J. Moon, T. W. Noh, *Phys. Rev. Lett.* **2018**, *120*, 136402.

[4] J. Chu, F. Wang, L. Yin, L. Lei, C. Yan, F. Wang, Y. Wen, Z. Wang, C. Jiang, L. Feng, J. Xiong, Y. Li, J. He, *Adv. Funct. Mater.* **2017**, *27*, 1701342.

[5] a) B. Konkena, J. Masa, A. J. R. Botz, I. Sinev, W. Xia, J. Koßmann, R. Drautz, M. Muhler, W. Schuhmann, *ACS Catal.* **2017**, *7*, 229; b) S. Xue, L. Chen, Z. Liu, H.-M. Cheng, W. Ren, *ACS Nano* **2018**, *12*, 5297; c) F. Wang, T. A. Shifa, P. He, Z. Cheng, J. Chu, Y. Liu, Z. Wang, F. Wang, Y. Wen, L. Liang, J. He, *Nano Energy* **2017**, *40*, 673; d) B. Song, K. Li, Y. Yin, T. Wu, L. Dang, M. Cabán-Acevedo, J. Han, T. Gao, X. Wang, Z. Zhang, J. R. Schmidt, P. Xu, S. Jin, *ACS Catal.* **2017**, *7*, 8549; e) Q. Liang, L. Zhong, C. Du, Y. Luo, Y. Zheng, S. Li, Q. Yan, *Nano Energy* **2018**, *47*, 257.

[6] C.-T. Kuo, M. Neumann, K. Balamurugan, H. J. Park, S. Kang, H. W. Shiu, J. H. Kang, B. H. Hong, M. Han, T. W. Noh, J.-G. Park, *Sci. Rep.* **2016**, *6*, 20904.

[7] a) J. Peng, J. Wu, X. Li, Y. Zhou, Z. Yu, Y. Guo, J. Wu, Y. Lin, Z. Li, X. Wu, C. Wu, Y. Xie, *J. Am. Chem. Soc.* **2017**, *139*, 9019; b) Z. Zeng, Z. Yin, X. Huang, H. Li, Q. He, G. Lu, F. Boey, H. Zhang, *Angew. Chem., Int. Ed.* **2011**, *50*, 11093; c) C. Tan, Z. Luo, A. Chaturvedi, Y. Cai, Y. Du, Y. Gong, Y. Huang, Z. Lai, X. Zhang, L. Zheng, X. Qi, M. H. Goh, J. Wang, S. Han, X.-J. Wu, L. Gu, C. Kloc, H. Zhang, *Adv. Mater.* **2018**, *30*, 1705509.

[8] P. Zhou, Q. Xu, H. Li, Y. Wang, B. Yan, Y. Zhou, J. Chen, J. Zhang, K. Wang, *Angew. Chem., Int. Ed.* **2015**, *54*, 15226.

[9] a) K. Li, D. Rakov, W. Zhang, P. Xu, *Chem. Commun.* **2017**, *53*, 8199; b) R. N. Jenjeti, M. P. Austeria, S. Sampath, *ChemElectroChem* **2016**, *3*, 1392.

[10] a) Z. Y. Xia, S. Pezzini, E. Treossi, G. Giambastiani, F. Corticelli, V. Morandi, A. Zanelli, V. Bellani, V. Palermo, *Adv. Funct. Mater.* **2013**, *23*, 4756; b) A. J. Cooper, N. R. Wilson, I. A. Kinloch, R. A. W. Dryfe, *Carbon* **2014**, *66*, 340; c) J. Li, C. Chen, S. Liu, J. Lu, W. P. Goh, H. Fang, Z. Qiu, B. Tian, Z. Chen, C. Yao, W. Liu, H. Yan, Y. Yu, D. Wang, Y. Wang, M. Lin, C. Su, J. Lu, *Chem. Mater.* **2018**, *30*, 2742; d) S. Yang, K. Zhang, A. G. Ricciardulli, P. Zhang, Z. Liao, M. R. Lohe, E. Zschech, P. W. M. Blom, W. Pisula, K. Müllen, X. Feng, *Angew. Chem., Int. Ed.* **2018**, *57*, 4677; e) Z. Huang, H. Hou, Y. Zhang, C. Wang, X. Qiu, X. Ji, *Adv. Mater.* **2017**, *29*, 1702372; f) Z. Lin, Y. Liu, U. Halim, M. Ding, Y. Liu, Y. Wang, C. Jia, P. Chen, X. Duan, C. Wang, F. Song, M. Li, C. Wan, Y. Huang, X. Duan, *Nature* **2018**, *562*, 254.

[11] B. Tian, B. Tian, B. Smith, M. C. Scott, R. Hua, Q. Lei, Y. Tian, *Nat. Commun.* **2018**, *9*, 1397.

[12] a) T. Sun, G. Zhang, D. Xu, X. Lian, H. Li, W. Chen, C. Su, *Mater. Today Energy* **2019**, *12*, 215; b) J. Jadwiszczak, C. O'Callaghan, Y. Zhou, D. S. Fox, E. Weitz, D. Keane, C. P. Cullen, I. O'Reilly, C. Downing, A. Shmeliov, P. Maguire, J. J. Gough, C. McGuinness, M. S. Ferreira, A. L. Bradley, J. J. Boland, G. S. Duesberg, V. Nicolosi, H. Zhang, *Sci. Adv.* **2018**, *4*, eaao5031.

[13] Z. Sun, Q. Liu, T. Yao, W. Yan, S. Wei, *Sci. China Mater.* **2015**, *58*, 313.

[14] H. Xu, J. Yi, X. She, Q. Liu, L. Song, S. Chen, Y. Yang, Y. Song, R. Vajtai, J. Lou, H. Li, S. Yuan, J. Wu, P. M. Ajayan, *Appl. Catal., B* **2018**, *220*, 379.

[15] H. Li, C. Tsai, A. L. Koh, L. Cai, A. W. Contryman, A. H. Fragapane, J. Zhao, H. S. Han, H. C. Manoharan, F. Abild-Pedersen, J. K. Nørskov, X. Zheng, *Nat. Mater.* **2016**, *15*, 48.

[16] M. S. Faber, M. A. Lukowski, Q. Ding, N. S. Kaiser, S. Jin, *J. Phys. Chem. C* **2014**, *118*, 21347.

[17] L.-A. Stern, L. Feng, F. Song, X. Hu, *Energy Environ. Sci.* **2015**, *8*, 2347.

[18] T. F. Jaramillo, K. P. Jørgensen, J. Bonde, J. H. Nielsen, S. Horch, I. Chorkendorff, *Science* **2007**, *317*, 100.

[19] J. Kibsgaard, Z. Chen, B. N. Reinecke, T. F. Jaramillo, *Nat. Mater.* **2012**, *11*, 963.

[20] J. N. Tiwari, S. Sultan, C. W. Myung, T. Yoon, N. Li, M. Ha, A. M. Harzandi, H. J. Park, D. Y. Kim, S. S. Chandrasekaran, W. G. Lee, V. Vij, H. Kang, T. J. Shin, H. S. Shin, G. Lee, Z. Lee, K. S. Kim, *Nat. Energy* **2018**, *3*, 773.

[21] J. Shi, X. Wang, S. Zhang, L. Xiao, Y. Huan, Y. Gong, Z. Zhang, Y. Li, X. Zhou, M. Hong, Q. Fang, Q. Zhang, X. Liu, L. Gu, Z. Liu, Y. Zhang, *Nat. Commun.* **2017**, *8*, 958.

[22] a) Y. Jiang, T. Sun, X. Xie, W. Jiang, J. Li, B. Tian, C. Su, *ChemSusChem* **2019**, *12*, 1; b) T. Sun, J. Wang, X. Chi, Y. Lin, Z. Chen, X. Ling, C. Qiu, Y. Xu, L. Song, W. Chen, C. Su, *ACS Catal.* **2018**, *8*, 7585; c) X. Li, Y. Fang, X. Lin, M. Tian, X. An, Y. Fu, R. Li, J. Jin, J. Ma, *J. Mater. Chem. A* **2015**, *3*, 17392; d) I. Ledezma-Yanez, W. D. Z. Wallace, P. Sebastián-Pascual, V. Climent, J. M. Feliu, M. T. M. Koper, *Nat. Energy* **2017**, *2*, 17031.

[23] Z. Zhuang, W. Sheng, Y. Yan, *Adv. Mater.* **2014**, *26*, 3950.

[24] J. Zhang, T. Wang, P. Liu, Z. Liao, S. Liu, X. Zhuang, M. Chen, E. Zschech, X. Feng, *Nat. Commun.* **2017**, *8*, 15437.

[25] J. P. Perdew, K. Burke, M. Ernzerhof, *Phys. Rev. Lett.* **1996**, *77*, 3865.

[26] G. Kresse, J. Hafner, *Phys. Rev. B* **1993**, *47*, 558.

[27] P. E. Blöchl, *Phys. Rev. B* **1994**, *50*, 17953.

[28] B. L. Chittari, Y. Park, D. Lee, M. Han, A. H. MacDonald, E. Hwang, J. Jung, *Phys. Rev. B* **2016**, *94*, 184428.

[29] S. L. Dudarev, G. A. Botton, S. Y. Savrasov, C. J. Humphreys, A. P. Sutton, *Phys. Rev. B* **1998**, *57*, 1505.

[30] S. Grimme, S. Ehrlich, L. Goerigk, *J. Comput. Chem.* **2011**, *32*, 1456.

[31] J. K. Nørskov, J. Rossmeisl, A. Logadottir, L. Lindqvist, J. R. Kitchin, T. Bligaard, H. Jónsson, *J. Phys. Chem. B* **2004**, *108*, 17886.

